ACS NANO

www.acsnano.org

ARTICLE

Electric-Field-Driven Assembly of Dipolar Spheres Asymmetrically Confined between Two Electrodes

Joseph R. Maestas, Fuduo Ma, Ning Wu,* and David T. Wu*

Cite This: *ACS Nano* 2021, 15, 2399−2412

Read Online

ACCESS | Metrics & More | Article Recommendations | Supporting Information

ABSTRACT: Externally applied electric fields have previously been utilized to direct the assembly of colloidal particles confined at a surface into a large variety of colloidal oligomers and nonclose-packed honeycomb lattices (*J. Am. Chem. Soc.* 2013, *135*, 7839−7842). The colloids under such confinement and fields are observed to spontaneously organize into bilayers near the electrode. To extend and better understand how particles can come together to form quasi-two-dimensional materials, we have performed Monte Carlo simulations and complementary experiments of colloids that are strongly confined between two electrodes under an applied alternating current electric field, controlling field strength and particle area fraction. Of particular importance, we control the fraction of particles in the upper *vs* lower plane, which we describe as asymmetric confinement, and which effectively modulates the coordination number of particles in each plane. We model the particle−particle interactions using a Stockmayer potential to capture the dipolar interactions induced by the electric field. Phase diagrams are then delineated as a function of the control parameters, and a theoretical model is developed in which the energies of several idealized lattices are calculated and compared. We find that the resulting theoretical phase diagrams agree well with simulation. We have not only reproduced the structures observed in experiments using parameters that are close to experimental conditions but also found several previously unobserved phases in the simulations, including a network of rectangular bands, zig zags, and a sigma lattice, which we were then able to confirm in experiment. We further propose a simple way to precisely control the number ratio of particles between different planes, that is, superimposing a direct current electric field with the alternating current electric field, which can be implemented conveniently in experiments. Our work demonstrates that a diverse collection of materials can be assembled from relatively simple ingredients, which can be analyzed effectively through comparison of simulation, theory, and experiment. Our model further explains possible pathways between different phases and provides a platform for examining phases that have yet to be observed in experiments.

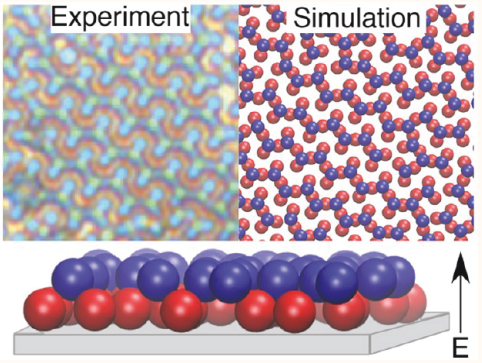

KEYWORDS: *directed assembly, self-assembly, confinement, dipolar colloids, electric field, Monte Carlo simulation*

Complex materials in nature are bottom-up assembled from simple constituents such as atoms and molecules. However, the inability to observe the mechanisms and interactions through which assembly occurs severely limits our ability to orchestrate the assembly of such materials. Colloids, which can be directly observed through optical microscopy, provide an excellent model system to gain a fundamental understanding of the mechanisms governing the assembly of molecules into intricate structures. Colloidal particles suspended in solution can self-assemble through relatively simple interactions, such as van der Waals, electrostatic, and steric interactions, to form complex and ordered structures.[1−4] While such kinds of intrinsic colloidal interactions can induce particle assembly, external stimuli are often used to experimentally control the attractive or repulsive interparticle interactions over a much wider range of distance and strength.[5−11] The ability to *direct* the assembly of colloidal particles into complex structures remains challenging, but could have important implications for advances in technologies such as photonic crystals and gels,[12−14] composite materials,[15,16] colloidal motors,[17−19] and metamaterials[20,21] as well as offer general strategies for creating complex ordered structures

Received: June 13, 2020
Accepted: January 22, 2021
Published: February 11, 2021

https://dx.doi.org/10.1021/acsnano.0c04939
ACS Nano 2021, 15, 2399−2412

of nanoparticles. As such, much research over the past decades has been dedicated to studying the equilibrium behavior of micron-sized colloidal particles in response to externally applied electric or magnetic fields.[11,22−28]

Geometric confinement can also dramatically influence colloidal interactions and assembly.[29−33] For example, both highly and weakly charged particles confined between surfaces show anomalous long-ranged attractions[34,35] whose theoretical origin has been debated for a long time.[36] The packing behaviors of both hard and highly charged spheres confined to a low-angle wedge geometry[37−40] are also significantly different from those observed in the bulk. Triangular, buckled, square, and staggered rhombohedral lattices have been reported. Geometric confinement has also been combined with external fields, which modulates the colloidal interactions and leads to structures unseen in the unconfined systems.[11,23,28,41,42] One notable example is that a pair of dipolar particles under strong confinement experiences a purely repulsive interaction with a shoulder that is less than two particle diameters in range. A collection of such particles, however, forms various types of complex condensed phases because of the so-called core-softened potential.[11,43,44]

In addition to experiments, computer simulations provide powerful tools to better understand the mechanisms governing colloidal assembly. Two- and three-dimensional (2D and 3D) colloidal systems have been studied extensively using Monte Carlo (MC),[33,44−47] molecular dynamics (MD),[48] and Brownian dynamics (BD) simulations.[49,50] For example, Camp[44] determined the phase behavior of colloidal disks interacting through core-softened repulsive interactions. He observed a fluid-lamellar-Kagome phase transition with increasing particle density. Hynninen *et al.*[46] found that 3D systems of dipolar hard spheres organized into stable regions of face-centered cubic, hexagonal close packed, and body-centered tetragonal crystals depending on both field strength and packing fraction. Gradner *et al.*[33] conducted MC simulations of colloids in a slit pore geometry and found that the confined colloids organized into layers and displayed crystalline order, while the unconfined colloids formed a stable liquid phase at the same conditions.

Our work here is motivated by previous studies of dipolar colloids under strong geometric confinement. In particular, we are interested in colloids interacting *via* a Stockmayer potential (which incorporates both dipolar and Lennard-Jones (LJ) interactions) that are highly confined between two electrodes, that is, whose separation is less than two particle diameters. As a result of the confinement, the particles separate into two layers that are near the top and bottom electrodes, respectively. An important feature of this work is that we vary the number ratio of particles near the top and bottom electrode, while previous work implicitly assumed a constant ratio of 1:1.[42,43,51] This means that in our work, the two parallel electrodes are not completely symmetric. As we will show later, this asymmetric confinement can be achieved by imposing a direct current (DC) electric field and inducing particle electrophoresis toward one of the electrodes. On the other hand, the variable particle ratios between top and bottom colloidal layers have also been observed in our recent experiments where Ma *et al.*[28] applied an alternating current (AC) electric field to induce phase transitions in solutions of polystyrene microspheres near one of the two indium tin oxide (ITO) electrodes by varying parameters such as field strength, frequency, and salt concentration. In the experiments, a large variety of elaborate structures including periodic arrays of colloidal oligomers and a nonclose-packed honeycomb-Kagome lattice have been obtained. The underlying mechanism governing the formation of these structures and their phase transitions, however, remains elusive. One important observation is that although the system itself was not geometrically confined (the separation between two electrodes was about 100 times of the particle diameter), upon the application of the electric field, particles were attracted toward the bottom electrode and stratified into bilayers where the number ratio of particles between two layers can be different from 1:1. The preferential assembly of a confined bilayer of particles rather than chaining along the field direction can lead to the formation of uncommon structures, such as thin-film photonic crystals, where the periodic particle array interacts with light and determines the properties of interest.

To better understand the previous experimental observations, we propose here a simplified colloidal system under strong geometric confinement and externally applied electric fields. We construct comprehensive phase diagrams as a function of the strength of dipolar interaction, particle area fraction, and the number ratio of particles between top and bottom layers. The phase diagrams compare favorably with those derived from theoretical calculations of the energies of several idealized lattices. Our simulations, when using comparable parameters to experiment, not only faithfully reproduce a large variety of complex structures that have been observed but also predict several previously unobserved phases including a network of rectangular bands, zig zags, and a sigma lattice. We carried out experiments at conditions corresponding to those in simulation and were able to observe all the predicted phases. In addition, our simulation work illuminates possible pathways between different phases and provides a framework for examining phases that have yet to be observed in experiments.

The Interaction Model. In the model used here, we include both LJ and dipolar interactions. The LJ interactions model long-range van der Waals attraction and short-range steric repulsion, while the dipolar interactions model the dipoles induced by the external electric field. Therefore, we model the interaction between particles i and j by the Stockmayer potential:

$$U(r_{ij}) = U_{LJ}(r_{ij}) + U_D(r_{ij}) \tag{1}$$

which includes both LJ and dipolar interactions:

$$U_{LJ}(r_{ij}) = 4\varepsilon\left[\left(\frac{\sigma}{r_{ij}}\right)^{12} - \left(\frac{\sigma}{r_{ij}}\right)^{6}\right] \tag{2}$$

$$U_D(r_{ij}) = \varepsilon'\left(\frac{\sigma}{r_{ij}}\right)^{3}[1 - 3\cos^2\theta] \tag{3}$$

where r_{ij} is the separation between particles i and j, ε is the LJ potential well depth, and σ is the distance where the potential is zero. The induced dipole moment of a particle is taken to be aligned with the externally applied electric-field direction (along the z-axis), and θ is the angle formed by the vector $\mathbf{r}_{ij}$ and the z-axis, as illustrated in Figure 1a. The parameter ε' characterizes the strength of the dipole−dipole interaction energy:

https://dx.doi.org/10.1021/acsnano.0c04939
ACS Nano 2021, 15, 2399−2412

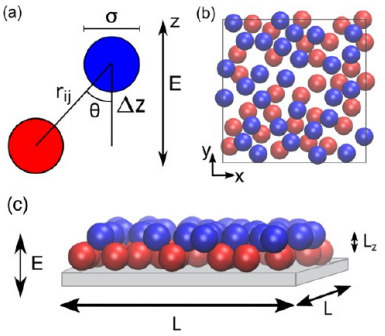

Figure 1. (a) Induced-dipolar interaction between particles. Particles with LJ size parameter σ are separated by a vector $\mathbf{r}_{ij}$ which forms an angle θ with the applied electric-field direction. Δz is the center-to-center difference in z-coordinates between particles located in the upper and lower planes. (b) Top view of the simulation box. (c) Side view of the simulation box. Particles in the upper (lower) plane are colored in blue (red). Simulation particles here and in figures below are depicted as spheres with diameter σ.

$$\varepsilon' = \pi \epsilon_m \epsilon_0 \sigma^3 |K|^2 {E_{rms}}^2/16 \quad (4)$$

where ϵ_m is the dielectric constant of the medium, ϵ_0 is the vacuum permittivity, K is the complex polarization coefficient, E_{rms} is the root-mean-square of the applied electric field $Ee^{i\omega t}$ (ω is the angular frequency of the AC electric field), and $|\cdot|$ represents the modulus of the complex number K. Except for low values of ε', which corresponds to low electric-field strength, the LJ attractive term of the Stockmayer potential is small compared to the dipolar interaction energy. As such, dipolar repulsion prevents particles in the same plane from overlapping, while short-range out-of-plane dipolar attractions are balanced by steric repulsion due to the LJ term. The LJ term in the Stockmayer potential thus primarily serves to set the effective size of the particles, through the LJ repulsion, and provides a magnitude of attraction in the limit of low dipolar strength.

Simulation Methods. The simulation box is a 3D slab (Figure 1b,c) with sides of length L and height L_z. The experimentally observed confinement of particles near the electrode surface into two distinct layers is modeled using two different models. In our first model, we fix the separation between the top and bottom layers of colloids to be $L_z = 0.7\sigma$. This value was chosen to match an average separation between the top and bottom layers of colloids under different experimental conditions[28] (Table 1, discussed below). We note that although the height of the experimental cell is ~100 times the particle diameter, the final structures observed typically form a bilayer of particles near the bottom substrate. The reason why particles are attracted toward the substrate upon the application of an external AC electric field is still unknown, although image−dipole−dipole interactions due to the conducting nature of the substrate could play a role. As the image−dipole interaction decays as $1/r$,[3] there is only a weak interaction between the upper layer of particles and the substrate, as compared with the image forces between the lower layer of particles and the substrate. As we do not explicitly include the substrate−particle interaction, but instead effectively account for the observed confinement of particles into a bilayer by fixing the z-coordinate of each particle to be in one of the two bilayer planes normal to the z-direction, we have also made the approximation to neglect the image forces in our model. We label particles in the upper plane blue and particles in the lower plane, closer to the bottom electrode, red. Experimentally, we observe that the particles in the upper plane "bond" to those in the lower plane and form close-packed clusters as a result of the out-of-plane dipolar attractions. While a range of separations between the upper and lower layers are observed in experiments,[28] the measured average separation in z-coordinates between neighboring particles in the two different planes, L_z, is ~0.7σ. This value of L_z yields an angle $\theta \sim 51.3°$ between neighboring particles in the two planes and the z-axis and reflects a balance of off-axis dipolar attraction (between top and bottom layer colloids) and in-plane repulsion (between particles in the same layer).

For simplicity, simulation parameters are reported in dimensionless variables, including the reduced temperature $T^* = k_B T/\varepsilon$ (T is the absolute temperature and k_B is Boltzmann's constant), the projected area fraction of particles $\eta = \frac{N\pi\sigma^2}{4L^2}$ where $0 \le \eta \le 2$, the reduced dipolar interaction strength $\lambda = \varepsilon'/\varepsilon$, and the ratio $\gamma = N_U/N_L$, of the number, N_U, of upper and, N_L, of lower plane particles, and where $N = N_U + N_L$ is the total number of particles. We also define a coordination number as the number of nearest-neighbor lower plane particles (red) coordinated with one upper plane particle (blue). In our second model presented later, we allow the particles to move continuously in the z-direction (but still restricted within a slab of height L_z) and use an external bias to control γ, while all other conditions are as previously described.

MC simulations of the above system are carried out in the canonical (NVT) ensemble using systems of $N = 60-735$ particles. The phase diagrams are mapped out using systems of $N = 60$ particles, while systems of $N = 240-735$ particles have also been studied to assess the effect of system size, whose

Table 1. Parameters Determined in Experiments and Used in MC Simulations for the Comparison of Different Phases Shown in Figure 9

		experiments			simulation		
structure type	γ	L_z/σ	λ	η	L_z/σ	λ	η
stripe	1:1	0.64 ± 0.10	7.86	0.44 ± 0.01	0.60	9	0.43
triangular bilayer	1:1	0.69 ± 0.08	16.05	1.08 ± 0.01	0.68	17	1.13
square bilayer	1:1	0.51 ± 0.06	16.05	0.92 ± 0.06	0.50	19	0.94
rectangular band	2:3	0.70 ± 0.09	4.01	0.82 ± 0.04	0.70	9	1.07
honeycomb-Kagome	2:3	0.56 ± 0.10	10.27	0.57 ± 0.02	0.70	10	0.71
zig-zag	1:2	0.66 ± 0.07	5.78	0.70 ± 0.03	0.66	15	0.70
sigma	1:2	0.32 ± 0.10	16.05	0.58 ± 0.01	0.50	16	0.64
tetramer crystal	1:3	0.61 ± 0.07	9.03	0.54 ± 0.01	0.68	11	0.54

https://dx.doi.org/10.1021/acsnano.0c04939
ACS Nano 2021, 15, 2399−2412

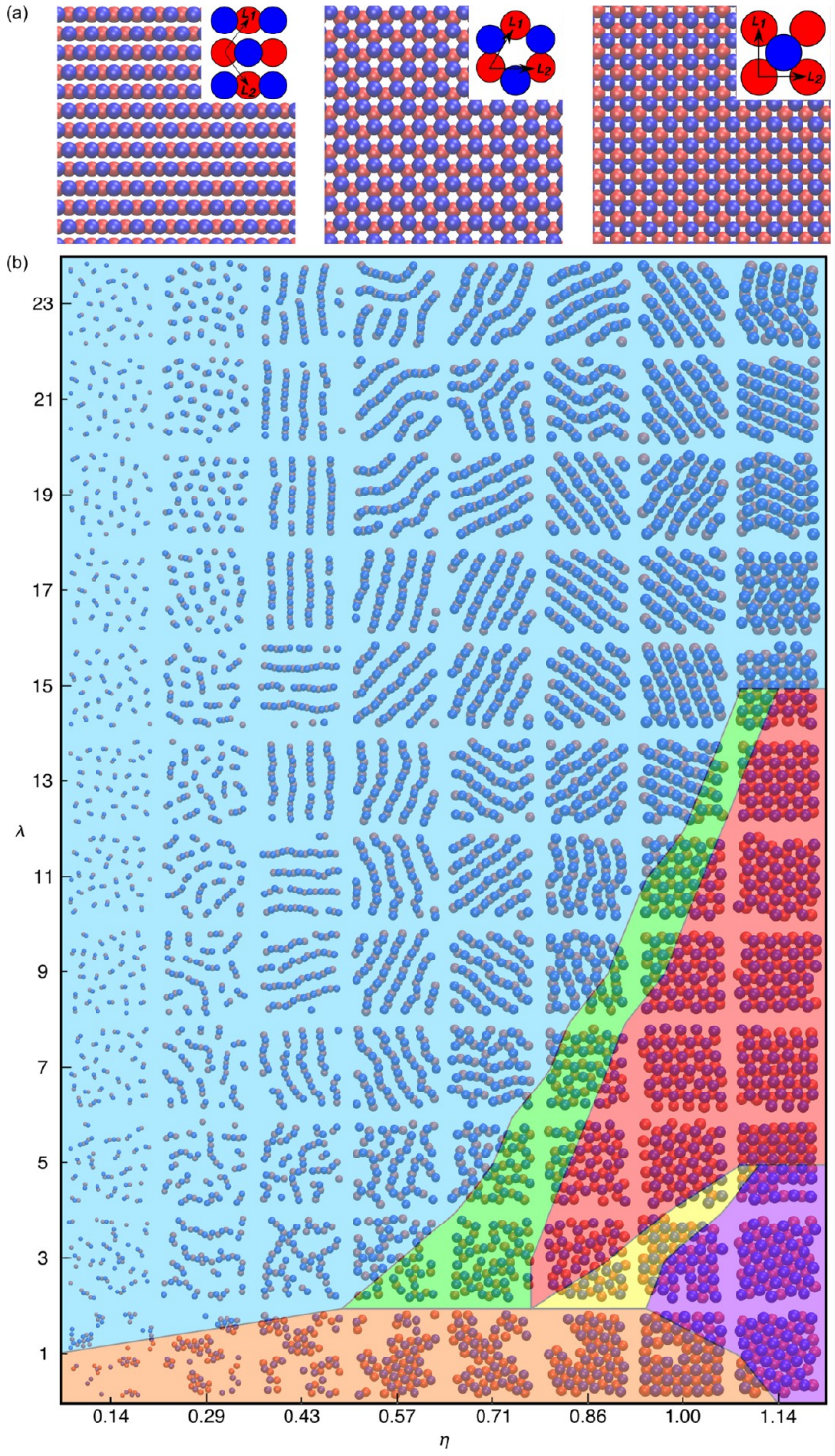

Figure 2. (a) Unit cells with lattice vectors, L_1 and L_2, for the idealized stripe, triangular, and square lattices used to calculate the theoretical phase diagram. (b) Simulated phase diagram for colloidal spheres under an AC electric field with $\gamma = N_U/N_L = 1$. The theoretically predicted phase diagram is overlaid on the simulation results, where the stripe (S), triangular bilayer (TB), and square bilayer (SB) phases are highlighted in blue, red, and purple, respectively. The regimes in green, yellow, and orange are the phase coexistence regimes S-TB, TB-SB, and S-SB, respectively.

results are consistent with the $N = 60$ systems. In the x and y dimensions, periodic boundary conditions are imposed, and the minimum image convention is used for particle interactions.[52] During the initial investigations of phase behavior, we find that when the reduced temperature T^* is low enough, we observe a variety of ordered phases, while fluid phases become more prevalent at higher T^*. Therefore, we chose a reduced temperature of $T^* = 0.35$ for all simulations, which is low enough for observing ordered structures, but high enough to allow equilibration within practical simulation times.

Most of the simulated structures can be characterized in terms of polygons. As shown in Figure S1a, we identify the

https://dx.doi.org/10.1021/acsnano.0c04939
ACS Nano 2021, 15, 2399−2412

upper plane particles as vertices, while a polygon edge is defined between two such vertex particles if both are within a distance less than or equal to a cutoff distance $r_c = \sigma$ from a commonly "bonded" lower plane particle. The number of polygons with different numbers of edges is counted (see Supporting Information for details) at different intervals throughout the course of the simulation. The number of polygons stabilizes for all pairs of λ and η after $\sim 7 \times 10^6$ MC steps, where we consider that the system reaches equilibrium and we set to be the minimum number of steps for our simulations. Simulation snapshots, created using VMD,[53] reflect the state of the system at that particular time. For each MC step, N randomly selected particles are sequentially moved in the x- and y-dimensions, while their z-coordinates were fixed. For every particle that is selected to move, the move is accepted or rejected according to the Metropolis algorithm:[54] If the change in system energy, ΔU, is negative, then the move is accepted; if ΔU is positive, then the move is accepted with probability given by the Boltzmann factor, $e^{-\Delta U/k_B T}$. The particle displacements in the x- and y- directions are each randomly selected from a uniform distribution ranging from $-d$ to d, where the maximum displacement, d, constant for a given simulation, ranges from 0.05σ to 0.30σ and is chosen so that approximately 30% of the moves are accepted.

Calculation of Energies for Idealized Lattice Structures. While the MC simulations provide equilibrium phases that minimize the free energy at a finite temperature, ground state phases at zero temperature are determined by calculating and comparing the energy of candidate idealized lattices. Specifically, the energies of perfect stripe, triangular, and square lattices seen for particle ratio $\gamma = N_U/N_L = 1$ (Figure 2a) are calculated, with particles interacting *via* the same Stockmayer potential used in the simulations (eq 1). Unit cells are defined for each of the above lattices with particle *1* located at the origin. Each unit cell is characterized by two lattice vectors plus additional vectors to any particles located within the unit cell (Figure 2a). The energy per particle of a lattice is calculated by summing the energy between particle *1* and all other particles j in the lattice:

$$U_{\text{lattice}} = \sum_{j \neq 1} u(\mathbf{r}_j - \mathbf{r}_1) \tag{5}$$

Each lattice is composed of a 400×400 grid of unit cells. The separation between particles in the x–y plane is dictated by the particle area fraction η, which is varied from 0.0285 to 1.14, with an increment of $\Delta\eta = 0.0285$. For the triangular and square phases, the particle separation within a unit cell is solely determined by the area fraction. In the stripe phase, however, the separation between neighboring particles along a single stripe, which sets the distance between neighboring stripes given the area fraction, is varied systematically for a given area fraction to find the energy minimum. The relative dipolar interaction strength λ is varied from 0 to 23 with $\Delta\lambda = 1$.

The energies of a series of finite lattices of increasing number of unit cells are calculated until the total energy converges. For all cases studied, the energy calculated using 400×400 unit cells differs from the energy calculated using 300×300 cells by <0.5%. As such, we use the calculation based on 400×400 unit cells to determine the lattice energies for the stripe, triangular, and square structures. A theoretical phase diagram (at zero T^*) is constructed by determining which lattice has the lowest energy as a function of λ and η. The Maxwell construction[55] was used to determine the two-phase coexistence regions.

The same approach of computing energies of candidate lattices to develop phase diagrams could be applied for the other particle ratios studied here besides $\gamma = 1$. However, due to the fact that there are many more phases observed for higher particle ratios, we have developed the analytical theory only for $\gamma = 1$ and studied the other particle ratios only with simulation.

RESULTS AND DISCUSSION

Simulation Results for Particle Ratio γ = 1:1. Many of the experimentally observed structures exhibit distinct number ratios of particles between the upper and lower planes, γ, which is an important parameter for dictating different phases even at similar electric-field conditions. Therefore, we first present the simulations with γ = 1:1. The first model, in which particles are explicitly confined to two planes along the z-direction, is used unless otherwise noted. The simulations detailed above are used to construct an approximate phase diagram by varying the reduced dipolar interaction λ and area fraction η at $T^* = 0.35$ for $N = 60$ particles. Since the simulations are conducted in the canonical ensemble (NVT), the different observed phases are not separated by a phase boundary curve, but by a coexistence region of some finite width. As our focus is to identify the phases in the phase diagram and also to compare them with experiment, we did not directly compute the width of these coexistence regions from simulation, for example by thermodynamic integration, although we do calculate the coexistence regions in the analytical model below.

Once the approximate regions of the observed phases are determined, simulations are then performed using 240 particles to identify more accurate phase regions, which are in good agreement with systems of 60 particles. We observe four predominant phases within the range of $1 < \lambda < 23$ and $0.14 < \eta < 1.14$, as shown in Figure 2b. In the low-area fraction regime ($\eta < 0.285$), a dilute gas phase of dimers and small oligomers is observed as a result of short-range out-of-plane dipolar attraction between particles in the upper and lower planes. Once these oligomers are formed, the long-range dipolar repulsion between particles within the same plane causes them to separate from each other. The boundary for this gas phase should vary with temperature, although we do not attempt to estimate it theoretically.

The oligomers assemble further as the area fraction is increased while minimizing the dipolar repulsion between neighboring particles. When λ is <3, the dipolar interaction is weak, and particles tend to condense into a square bilayer even at relatively low-area fraction, leading to a broad two-phase coexistence region of square bilayer solid with the gas phase. At higher values of λ and intermediate values of η ($0.285 < \eta < 1.000$), a stripe phase consisting of longer chains begins to form. At this intermediate density, the dipolar attraction between particles in different planes stabilizes the formation of colloidal chains that are formed by an alternating arrangement of upper (blue) and lower (red) particles, while the long-range repulsion between neighboring chains keeps them separated from each other to minimize the overall free energy. This is further evidenced by noticing that two neighboring chains are offset by one particle, that is, a blue particle in one chain is closest to a red particle in the neighboring chain. This configuration minimizes the dipolar repulsion between two chains. To accommodate even higher particle area fraction, the stripes have to bunch closer. This, however, increases the

https://dx.doi.org/10.1021/acsnano.0c04939
ACS Nano 2021, 15, 2399−2412

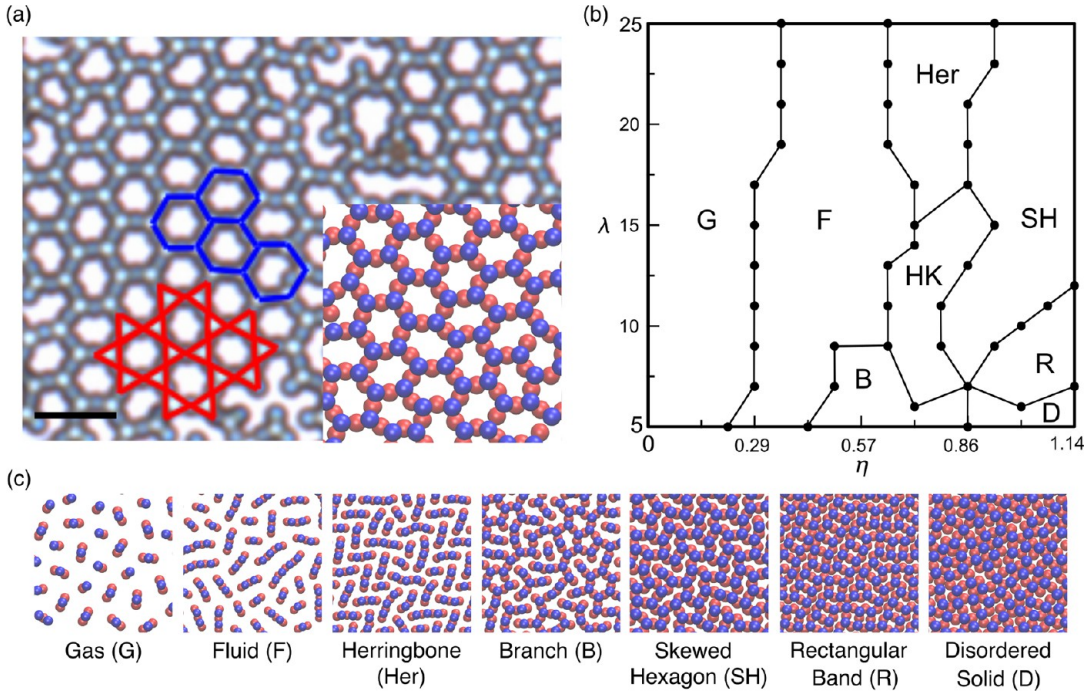

Figure 3. (a) The HK structure observed in experiments (adapted with permission from Figure 5a in ref 28, Copyright 2013 American Chemical Society), where the upper-layer honeycomb and lower-layer Kagome lattices are highlighted in blue and red lines, respectively. Inset: The HK structure obtained from the MC simulation. Scale bar: 10 μm. (b) The phase diagram for γ = 2:3. The black dots represent estimated phase boundaries based on simulation results. (c) Snapshots of the simulated phases.

energetic penalty due to stronger dipolar repulsion between particles in the same plane. To compensate, the particles have to maximize the energetic gain from dipolar attraction between blue and red particles. As a result, each blue particle bonds to three red ones instead of two and the stripe phase gradually changes into triangular bilayers. Although we do not simulate this for higher values of λ, it is reasonable to expect that the coordination number for the blue particles can be further increased to four as η increases further and a square bilayer would eventually become more favorable.

To further understand the appearance of the stripe, triangular, and square phases, we calculate their respective theoretical zero-temperature energy surfaces as a function of λ and η. The energy surfaces of the stripe, triangular, and square phases were plotted together, and the minimum energy structure at each pair of λ and η, accounting for two-phase coexistence regions using the Maxwell construction, can be identified as the thermodynamically stable phase. Note that at zero temperature, the gas phase region collapses to a vacuum line. We overlay this theoretical phase diagram on the simulation results as shown in Figure 2b, with the stripe phase shown in light blue, the triangular bilayer in red, and the square bilayer in purple. The coexistence between the stripe and triangular bilayer phases, triangular bilayer and square bilayer phases, and stripe and square bilayer phases is shown in green, yellow, and orange, respectively. Overall, the simulated and theoretically predicted phases and regions of coexistence are in excellent agreement over the wide range of parameters studied. In particular, the coexistence region between the triangular and square bilayers is consistent with simulation results for all values of η and λ. At low values of λ, our simulations show a coexistence of gas phase of oligomers and square bilayers. Interestingly, the same feature is also captured by our theoretical calculation, but between a very dilute stripe (approximating a gas) and square bilayer phases. The boundary between the stripe and triangular bilayer matches well with simulation for most values of η and λ. For η = 1.14 and λ = 15−17, the theoretical phase boundary differs slightly. As shown in Figure S2, we calculate the contributions in energies from the nearest neighbors and next-nearest neighbors, for each phase as a function of area fraction η and dipolar interaction strength λ. For a constant λ and low η, the dipolar interaction between nearest neighbors is attractive only in stripes, because blue and red particles can be almost tangent to each other along the single stripe. In addition, the separation between stripes can be large enough to minimize the dipolar repulsions. Therefore, a stripe phase is energetically favorable in this region. As η increases, adjacent stripes are forced to be closer. As a result, the stripe phase can become energetically unfavorable compared with the triangular and square bilayers, where the dipolar interactions between the nearest neighbors become attractive and stronger than those in stripes since the coordination numbers between blue and red particles are larger: 3 for triangle and 4 for square. Therefore, triangular and square phases become more favorable at intermediate and high area fractions.

The Effect of γ on the Phase Diagram. One of the most notable structures discovered in the previous experiments is the formation of a combined honeycomb and Kagome (HK) network.[28] As highlighted in Figure 3a, the particles in the lower plane, which appear darker, form into a Kagome lattice (indicated by the red lines), while those in the upper plane, which appear brighter, arrange into a honeycomb lattice (indicated by the blue lines). Combining both planes, we can see that every honeycomb edge contains one Kagome site, while every Kagome triangle contains a honeycomb site. Although a Kagome lattice had also been obtained by overnight self-assembly of Janus spheres with three patches,[56]

https://dx.doi.org/10.1021/acsnano.0c04939
ACS Nano 2021, 15, 2399−2412

this crystallization process is very slow, and the tripatchy particles are tedious to fabricate. In contrast, our more complex structures are formed from isotropic building blocks within seconds in response to an external AC electric field.[28] Motivated by this highly surprising and porous structure, we investigate its formation mechanism *via* MC simulations. We note that in the ideal HK structure, the upper-layer to lower-layer particle ratio is γ = 2:3, since each top particle bonds to three bottom particles and each bottom particle bonds with two top ones. Therefore, we perform simulations for γ = 2:3 at different values of η and λ, and the phase diagram is shown in Figure 3b. As discussed above, we did not calculate the widths of the coexistence regions, and so the lines in the phase diagrams are not to be taken to be exact phase boundaries, but rather the approximate location of where there is a change in observed phase. These boundaries are estimated from the observed simulation phases and located up to the interval resolutions of the simulation parameters. In particular, the intersection of phase boundary lines at a point should not be taken to identify triple or higher-order points. While the regions of phase coexistence could in principle be determined using thermodynamic methods as demonstrated previously, the complexity of the phase diagram makes such computation extensive, and our goal was to identify the different phases that might be observed in experiments.

A dilute gas phase (G) of dimers and trimers can be observed at low-area fractions (η < ~0.285). A fluid phase (F) of longer oligomers, mostly pentamers with γ = 2:3, is observed for intermediate area fractions (0.285 < η < 0.570). A herringbone-like (Her) structure appears as area fraction and reduced dipolar interaction are increased. In comparison, the branched networks (B) form at the intermediate area fraction and low dipolar interaction region of the diagram (η ~ 0.570 and λ < 10). The coordination number of the particles in the upper plane (blue) also changes from 2 to 3. The combined honeycomb-Kagome lattice (HK, inset of Figure 3a) is observed in the region of intermediate area fraction and dipolar interaction, that is, 5 < λ < 15 and 0.570 < η < 0.855. This highly porous but ordered structure arises in this phase space because it maximizes the dipolar attraction between blue and red particles by forming small tetrahedra with a high coordination number of 3 while minimizing the dipolar repulsion between red particles by arranging them far from each other. The transition to other phases surrounding the honeycomb-Kagome lattice can be understood in terms of changes in packing and also its influence on the coordination number. As the area fraction is further increased, the herringbone and honeycomb-Kagome structures begin to buckle into a network of skewed hexagons (SH), where each hexagon is tilted 90° from its neighbors. A rectangular band structure (R) appears for λ < 15 and η > 0.860, where the particles orient into alternating bands of long and short rectangles. A final phase composed of tetramers and pentamers packed into a disordered solid (D) is observed in the high-area fraction and weak dipolar interaction region (η > 0.855 and λ < 7).

We have also constructed the phase diagrams for γ = 1:2, 1:3, and 1:4, which are shown in Figures 4–6. Dilute phases of monomers, dimers, and trimers are always prevalent in the low-area fraction regime. Structures with more order and higher coordination number begin to emerge as the area fraction is gradually increased. For example, at higher values of λ, the low-area fraction gas phase of trimers seen in Figure 4 for γ = 1:2

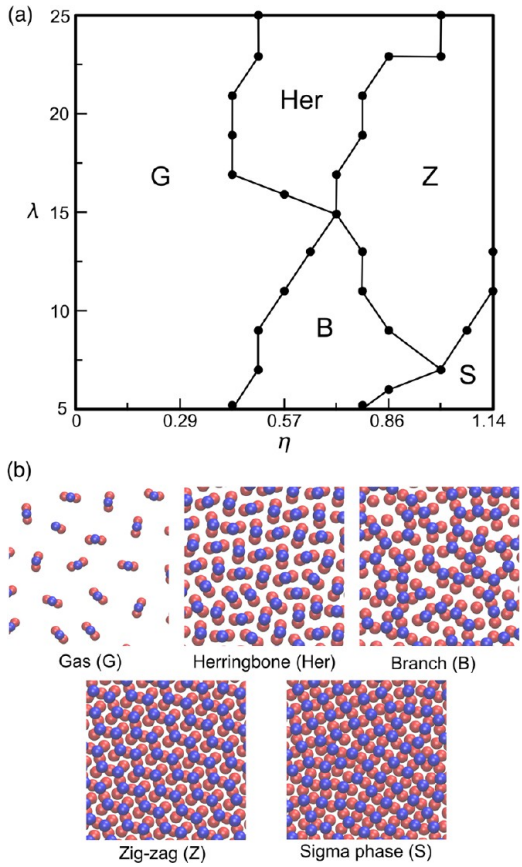

Figure 4. (a) The phase diagram at γ = 1:2. The black dots represent estimated phase boundaries based on simulation results. (b) Snapshots of five different phases observed.

begins to change into a herringbone-like structure and then a phase of zigzag stripes (Her and Z in Figure 4b) since stronger dipolar interaction and higher area fraction favor additional bonding between blue and red particles and the coordination number for the blue particles changes from 2 to 3. Although the herringbone-like phase of trimers (Her) easily satisfies the constraint of a top-to-bottom particle ratio of 1:2, the zigzag stripes have to arrange in a way that every blue particle bonds to three red particles, while the red particles alternate between bonding to either one or two blue particles, giving an average coordination number of 1.5. This is in contrast with the stripe phase at the same η and λ shown in Figure 2, where a straight and alternating arrangement of red and blue particles satisfies the ratio of γ = 1:1. It shows the impact of γ when the other parameters η and λ are kept constant. With relatively weak dipolar interactions, a branched network (B) forms in the intermediate area fraction regime, while a Frank–Kasper sigma phase[57,58] (S in Figure 4b) can be observed within a narrow regime of high-area fractions (η > 0.7125 and λ < 10), which is nontrivial to form from particles with only simple interaction potentials.

For particle ratios γ = 1:3 and γ = 1:4, both gas phases are primarily a mixture of trimers and monomers (with composition controlled by γ), and the fluid phases are dominated by tetramers for γ = 1:3 (Figure 5a) and a 1:1 mixture of tetramers and monomers for γ = 1:4 (Figure 6a). This indicates that as area fraction increases, the dipolar repulsion between red particles forces them to bond more strongly with the blue particles so that the coordination

https://dx.doi.org/10.1021/acsnano.0c04939
ACS Nano 2021, 15, 2399–2412

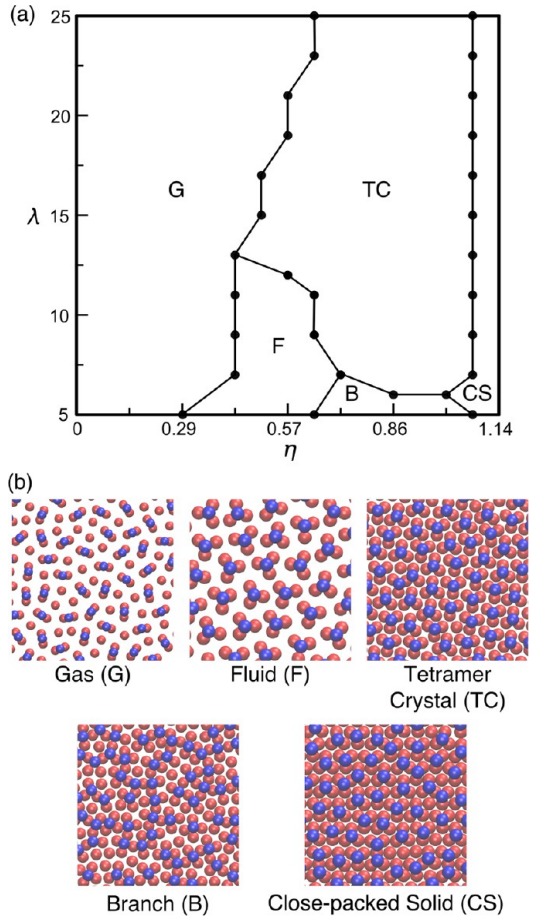

Figure 5. (a) The phase diagram at γ = 1:3. The black dots represent estimated phase boundaries based on simulation results. (b) Snapshots of five different phases observed.

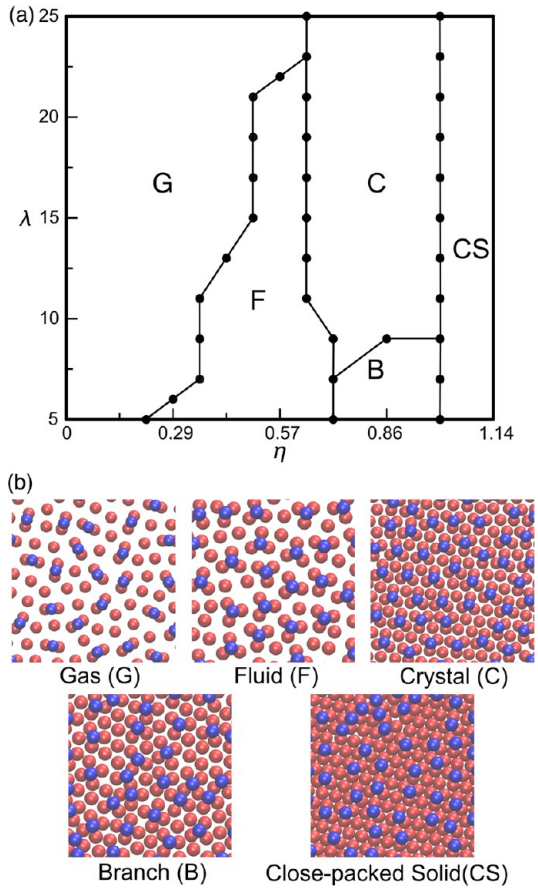

Figure 6. (a) The phase diagram at γ = 1:4. The black dots represent estimated phase boundaries based on simulation results. (b) Snapshots of five different phases observed.

number increases from 2 to 3. The crystalline phases for both cases are also dominated by tetramers except that there are unbonded red particles in the crystalline phase for γ = 1:4 to satisfy the particle ratio constraint. In the high-area fraction regime, the particles in the lower layer are nearly close packed. While order in the upper layer is still apparent for γ = 1:3, the blue particles are disordered for γ = 1:4 and partially disordered for γ = 1:3.

Controlling the Particle Ratio γ by a DC Electric Field. As shown in the preceding section, the observed phases are very sensitive to γ, the number ratio of particles located in the upper plane to the lower plane. For example, when γ = 1:3, clusters of tetramers where each upper plane particle coordinates with exactly three lower plane particles are more likely to form. At the same γ, however, the honeycomb-Kagome structure is not observed since its formation requires two upper plane particles to coordinate with three lower plane particles simultaneously. By fixing the ratio γ in our simulations, we introduce a constraint on the particle distribution between the upper and lower planes, where different phases can be controlled. In our previous experiments,[28] however, this number ratio is not controlled purposely but dictated by the particle concentration and interactions between particles and substrate. For example, upon the application of the electric field, we find that all particles in the bulk are attracted toward both electrodes and stratify into two layers near each of them spontaneously. While the tendency to form two layers could be due to image dipole−dipole interaction between the polarized particle and the electrode, the true nature of this particle−substrate attraction remains elusive. At relatively high particle concentration, the substrate can be saturated by particles that are initially close to it, and additional ones arriving from the bulk have to be maintained in the upper plane. Note that we purposely controlled the particle concentration in experiments so that structures with more than two layers were avoided. Therefore, in experiments, both the particle−substrate interaction and particle concentration contribute to the observed ratio γ, which in turn determines the possible phases.

Here, we propose a second model that can control the ratio γ precisely. We hypothesize that this can be achieved by introducing a DC bias across two electrodes that induces the electrophoretic motion of particles toward the substrate. It can be modeled by a simple attractive potential along the z-direction:

$$U_{\text{substrate}}(z_i)/k_BT = 2Fz_i/\sigma \tag{6}$$

where z_i is the separation between particle i and the substrate, σ is the particle diameter, and F represents the reduced drag force (scaled by k_BT/σ) on the particle caused by electrophoresis, that is, $F = 3\pi\epsilon_0\epsilon_m\zeta_pE_{DC}\sigma/k_BT$ (where ζ_p is the particle zeta potential and E_{DC} is the DC electric-field strength). While the first model effectively has two different species (one in each layer) and thus two corresponding chemical potentials, this second model apparently only has

https://dx.doi.org/10.1021/acsnano.0c04939
ACS Nano 2021, 15, 2399−2412

one. This chemical potential sets the total number of particles and corresponds to the total chemical potential of the first model. By specifying the attractive force in the z-direction, and given that the particle positions are always very close to one of two values (for the two planes), the particles in the two planes differ by a constant potential energy due to the applied field. Specifying this potential difference is equivalent to specifying the difference in chemical potentials in the first model. Thus, the two models are thermodynamically equivalent, with the first model corresponding to an ensemble with fixed particle ratio and the second model corresponding to an ensemble with fixed chemical potential difference between the two layers. By introducing this effective attraction, we allow particles to move continuously in the z-direction (confined in a slab of $L_z = 0.7\sigma$) and can relax the constraint for particle distribution between two confined electrodes. As the number of particles attracted to the substrate increases, the dipolar repulsion between them sets the limit of available space for particles at the lower plane, and an equilibrium between the number of upper plane and lower plane particles can be established. We show here that γ can be effectively controlled by changing the magnitude of this attractive force, F, to the substrate.

As with the simulations above, all particles are initially confined between two electrodes corresponding to $L_z = 0.7\sigma$. Although the initial value of γ is set to be 1:1, as we will show later, its final value can be controlled by F. All particles are now allowed to displace along the z-direction, although still confined within the box height L_z to remain consistent with the experimental observation of the tendency to form two layers. After approximately 10^5 MC steps, the particles spontaneously organize into two layers with a different equilibrium particle ratio γ by tuning F for a given pair of λ and η. Figure 7 shows the particle ratio γ plotted as a function

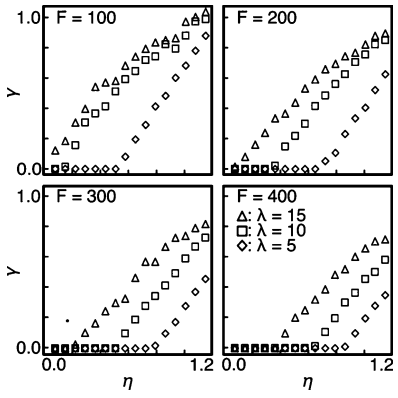

Figure 7. Impact of F on controlling the particle ratio γ between the upper and lower planes. (a) F = 100, (b) F = 200, (c) F = 300, and (d) F = 400.

of area fraction for several different values of λ and F. When F is relatively weak, the value of γ can be tuned within the full range of 0−1 at relatively high λ (Figure 7a). This is because strong dipolar repulsion between particles on the substrate forces more particles to stay in the upper plane. On the other hand, when λ is small (*e.g.*, $\lambda = 5$), essentially all particles will be located at the bottom substrate ($\gamma = 0$) if the area fraction is also small. Particles can only be in the upper plane when the substrate is fully saturated at higher area fractions. As F is gradually increased from 200 to 400, particle attraction to the substrate begins to dominate, and the upper limit of γ that can be achieved decreases from 0.9 to 0.7 (Figure 7b−d). In general, higher values of λ allow continuous variation of γ with η, while a weaker dipolar interaction leads to a fully saturated substrate before filling the upper layer.

We confirm that all phases simulated by using a fixed γ initially can also be reproduced by setting an appropriate value of F. The comparison of a few representative phases obtained from these two different methods including the triangular bilayer, the honeycomb-Kagome, the zigzag stripe, and tetramer crystal with different values of γ are shown in Figure 8. In the right-hand column of Figure 8, histograms of the z-coordinates verify that the particles organize into primarily two positions, separated by $\Delta z \sim 0.7\sigma$. The peaks' heights clearly demonstrate that γ can be tuned by F. Therefore, the application of an additional DC electric field, which is experimentally implementable, will allow us to precisely control the number ratio of particles located between lower and upper planes.

Comparison between Simulation and Experimental Results. In our previous experiments, colloidal particles exhibit a large and stunning variety of structural changes in response to different electric-field strengths and particle concentrations.[28] In this work, we have also observed a rich assortment of phases *via* MC simulation using idealized parameters. Several previously unobserved phases, including the rectangular bands, zig zags, and sigma lattice, were first identified in our simulations and later observed in experiments at corresponding conditions. Examples of notable structures observed are shown in Figure 9. Here, we aim to compare our simulation results with experimental observation using the same experimental parameters. In order to make a faithful comparison to simulation results, we evaluate all simulation parameters based on experimental conditions. We equated the LJ diameter σ to the estimated geometric diameter, D, of the spherical particle. The field strengths are measured in experiments. They are used to calculate $\lambda = \varepsilon'/\varepsilon$ at room temperature (T = 298 K) for each experimental phase based on eqs 4, 7, and 8. The LJ energy, ε, is estimated based on the reduced temperature used in simulation (T^* = 0.35, T = 298 K, and $\varepsilon = k_B T/T^* = 1.17 \times 10^{-22}$ J). The temperature is set low enough that the LJ energy does not affect the resulting structure very much, which is a reasonable expectation for the formation of crystal phases. The dipole moment p of a particle is given by

$$p = \frac{1}{2}\pi\epsilon_0\epsilon_m D^3 |K| E_{rms} \tag{7}$$

which relates the experimental dipolar interaction to our simulation dipolar interaction *via* eq 8:

$$U_D(r_{ij}) = \frac{p^2}{4\pi\epsilon_0\epsilon_m r_{ij}^3}[1 - 3\cos^2\theta] = \varepsilon'\left(\frac{\sigma}{r_{ij}}\right)^3[1 - 3\cos^2\theta] \tag{8}$$

with the dipolar interaction energy ε' given by eq 4. The complex polarization coefficient[59] K depends on the particle diameter, field frequency, Debye length κ^{-1}, and particle zeta potential ζ_p, which can all be measured experimentally.[60−62] We calculate K based on the modified Dukhin−Shilov theory,[62] which captures the dielectric dispersion within the low-frequency regime (500−10,000 Hz) that we are interested in. The separation between upper and lower plane particles L_z and the area fraction η are also determined from the

https://dx.doi.org/10.1021/acsnano.0c04939
ACS Nano 2021, 15, 2399−2412

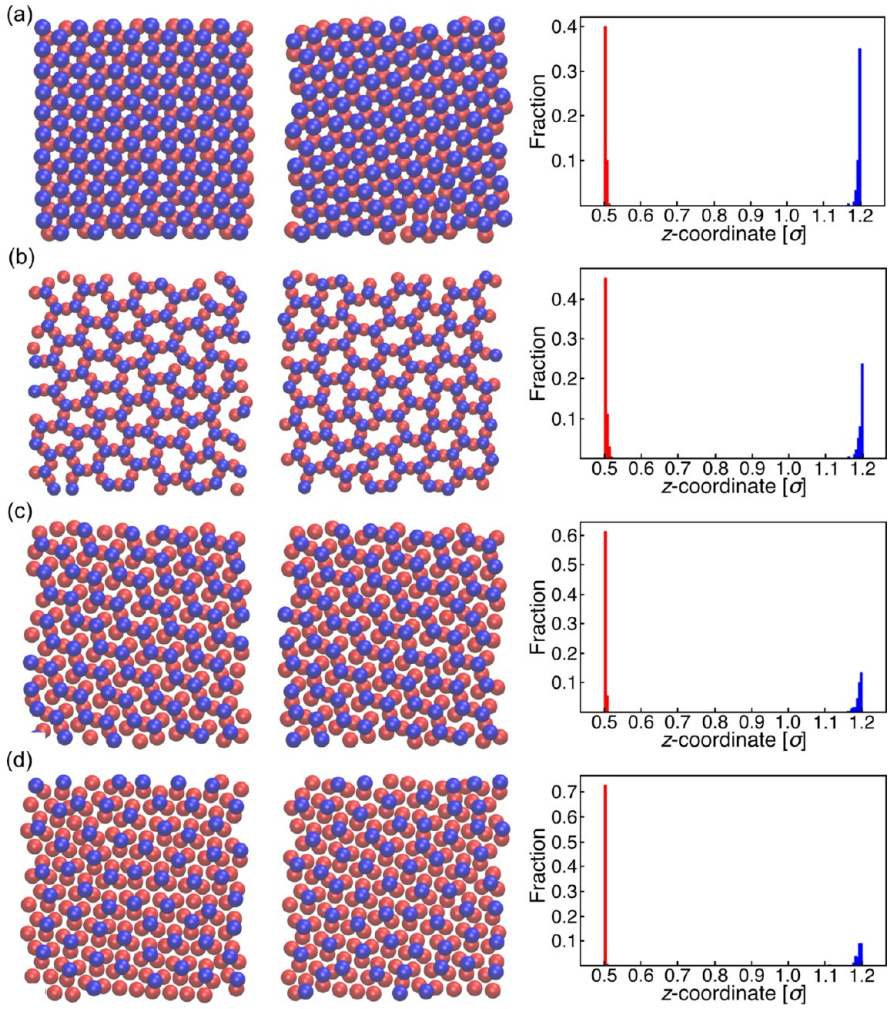

Figure 8. Comparison between simulations using a fixed γ (left column) and simulations where γ is controlled by an external bias (middle column). Histograms of the particle z-coordinates from the configurations shown in the middle column demonstrate that the upper and lower layers are separated by $\Delta z \sim 0.7\sigma$ and that γ can be tuned using an external bias (bias increases from a−d) (a) triangular bilayer (F = 100, γ = 1:1, λ = 10, η = 1.14), (b) honeycomb-Kagome (F = 120, γ = 2:3, λ = 10, η = 0.71), (c) zigzag stripe (F = 355, γ = 1:2, λ = 20, η = 0.86), and (d) tetramer crystal (F = 700, γ = 1:3, λ = 15, η = 0.86).

experimental images. Specifically, L_z is calculated by measuring the projected separation between neighboring particles in two different planes using ImageJ,[63] and they are assumed to be tangent to each other based on our previous experimental observation.[28] We use this value of L_z to set (in our first model) or limit (in our second model) the z-coordinates of all particles in the simulations. In a few cases, the simulation parameters have been further adjusted to find the same phase that matches experiments. The experimental and simulation parameters for different types of structures are summarized in Table 1.

We used these parameters that correspond to the experimental conditions in simulations of N = 240 particles. We use the ideal unit cell of the dominant observed phase in assigning γ from experiments, rather than including the count from minor regions or defects. Thus, for example, in a typical experiment corresponding to γ = 1:1, only minor regions within the total experimental sample have $\gamma \neq$ 1:1. As shown in Figure 9, many of the phases observed in experiments are successfully modeled by a Stockmayer potential. Clearly, the similar microstructure between the experiment and simulation results is indicative of good qualitative agreement between the two methods. Furthermore, the differences between experimental conditions and simulation parameters varied by <20% in most cases (Table 1). In particular, the stripe, triangular, square, and tetramer phases have been simulated using λ, η, and L_z that are within 20% error from those measured experimentally. The λ used to simulate the honeycomb-Kagome and sigma phases are within 3% error from the experimental values, while L_z and η were tuned. For the rectangular band and zigzag phases, the values of λ were varied in simulation from those determined in experiments, while keeping the experimental values of L_z and η. Several factors could possibly contribute to the discrepancies between experimental and simulation results. The particles used in experiments have a finite size, and the polarization would be extended across the entire particle volume, whereas the point dipole approximation used in the simulation is more appropriate for the far field. In addition, a particle that gains a dipole moment also generates an electric field that affects all neighboring ones. Here, we do not account for this collective polarization in our model.[64,65] We estimate the dipolar repulsion between two particles at contact when mutual polarization is considered. It is different from the one that we

https://dx.doi.org/10.1021/acsnano.0c04939
ACS Nano 2021, 15, 2399−2412

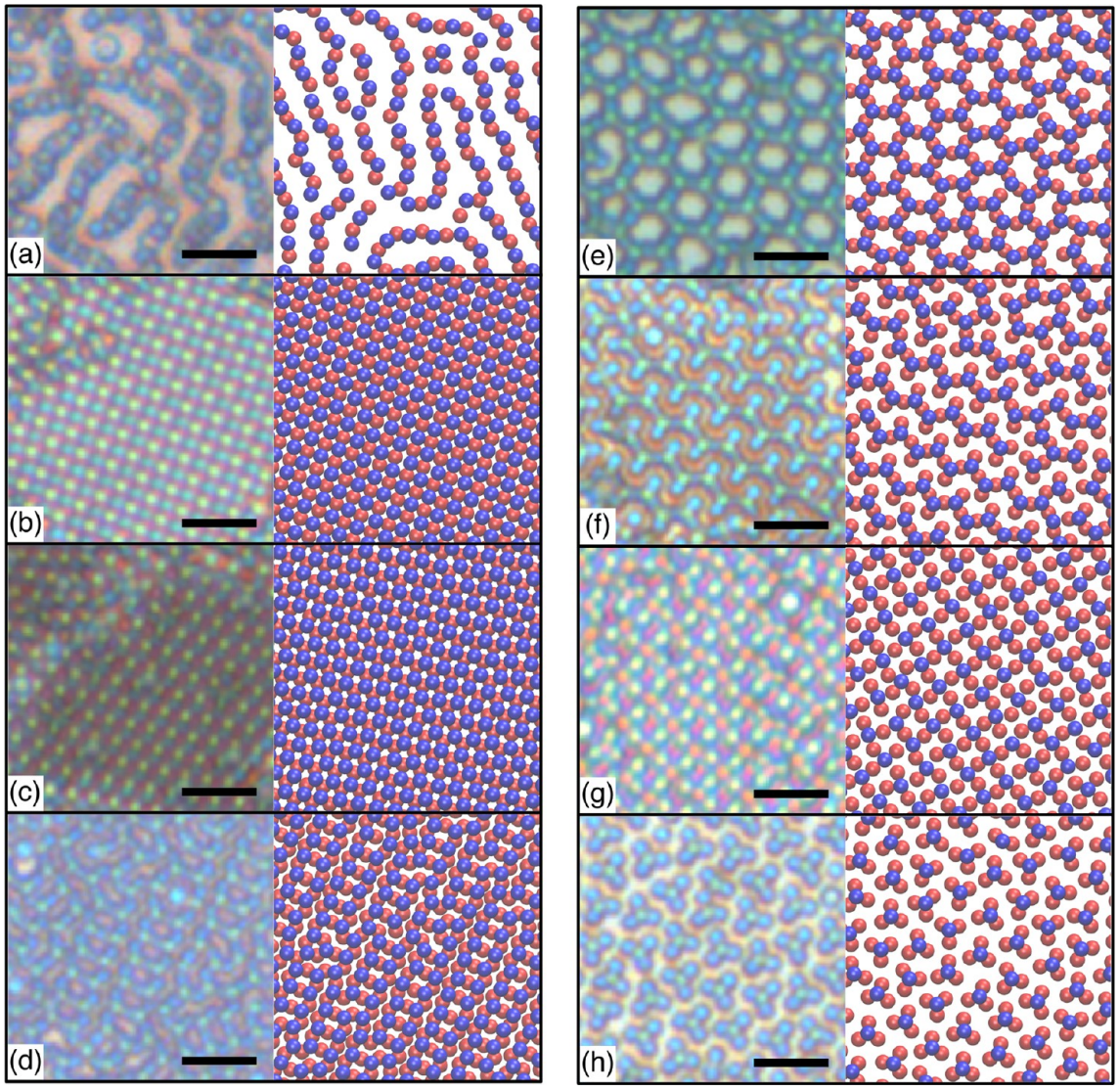

Figure 9. Using a relatively simple model, we found exceptional agreement between experimental (left) and simulation (right) results. Particles used in the experiments were PS and were 1.2 μm in diameter, and simulation particle diameters were chosen to match experiment. Some of the phases observed were (a) a worm-like phase, (b) a square bilayer, (c) a triangular bilayer, (d) rectangular bands*, (e) a honeycomb-Kagome structure, (f) a lattice of zig zagged stripes*, (g) a sigma lattice*, and (h) a network of tetramers. Asterisked phases were identified first in simulation and then observed in experiment at the corresponding conditions. Scale bars: 5 μm. A comparison between experimental conditions and simulation parameters is detailed in Table 1.

are using in eqs 7 and 8) by 5%. Therefore, the impact of mutual polarization is small. In addition, our model imposes geometric confinement between two electrodes, while in the experiments, the separation between two electrodes is much larger than a few particle diameters, although the applied electric field confines the final colloidal structures into bilayers potentially due to additional electrode-substrate interactions. Based on the generally good agreement between simulated and experimentally observed phases, these additional details, however, appear to be relatively minor.

We also find that the degree of confinement plays an important role in the type of structure that can be modeled. Although the honeycomb and sigma lattices have been successfully simulated using several values of L_z, they become increasingly difficult to form as L_z is decreased. This is likely a limitation of the model, as the orientation-dependent dipolar interactions become more repulsive as L_z is decreased. Indeed, we have estimated that a close-packed tetramer ($L_z = \sqrt{2/3}\,D$) has the lowest energy if we only consider the dipolar interactions. In our experiments however, the sigma phase (and tetramers) is observed to form with a $L_z = 0.3 \pm 0.1D$ between particles in two planes. In this case, the angle θ between the particles and the electric field is $\theta \sim 72.5°$, which should clearly lead to repulsive dipolar interactions between the particles. This indicates that other phenomena such as interactions due to electrohydrodynamic (EHD) flow are contributing to the formation of the sigma lattice. For example, under our experimental conditions, the EHD flow is very likely extensile,[66] which generates repulsion between bottom particles and attraction between top and bottom particles. Such an interaction will allow for the formation of experimentally observed stable tetrameric clusters where the petals are well separated and L_z is small. The impact of EHD interactions will be considered in our future studies.

https://dx.doi.org/10.1021/acsnano.0c04939
ACS Nano 2021, 15, 2399−2412

CONCLUSIONS

The directed assembly of dipolar colloidal spheres confined between two electrodes under an AC electric field is investigated by Monte Carlo simulations and simple analytical theory and quantitatively compared with corresponding prior and supplemental experiments. Using the Stockmayer potential, which captures the effect of dipolar interactions between colloids, we map out a rich assortment of 2D phases that have been observed in previously reported experiments. Our model is further validated by the discovery of several structures, including a rectangular band phase, a network of zig zags, and the sigma lattice, which were first identified in simulation and then confirmed in experiment at corresponding conditions. In particular, we report the phase diagrams as a function of electric-field strength and area fraction for various ratios of upper plane to lower plane particles. This ratio γ, which represents the degree of asymmetry in the confinement, acts to control the coordination number and is found to play a critical role in determining the classes of structures observed in the assembled quasi-2D materials. While previous work on confined colloids has explored the symmetric case where γ = 1:1, we vary γ in our work, which allows tuning of the coordination number between upper and lower plane particles. As such, we observe a number of complex phases including a honeycomb-Kagome network, an alternating pattern of short and long rectangular bands, a network of zig zagged stripes, and a sigma lattice. The phase diagram based on analytical theory for the energies of perfect stripe, triangular, and square lattices is in excellent agreement with the phase boundaries estimated from simulations, suggesting the dominance of enthalpic contribution in different phases for these conditions. Further simulations based on this simple geometry and particle interaction have also been performed in an attempt to explain different types of structures observed experimentally, where particle confinement apparently results from electrode surface attractions. Interestingly, by using parameters measured directly from experiments, we find very good agreement between many of the observed and simulated structures, validating our relatively simple model. As the phase diagrams are very sensitive to the particle ratio in different planes, there are likely many other phases that can be observed. Therefore, we hope to use the knowledge gained through this work as guidance to discover structures in future experiments. As such, the model presented here establishes a framework for analyzing phase transitions for a variety of experimental parameters and provides a better understanding of the electric-field-driven assembly of colloids.

EXPERIMENTAL METHODS

The experimental methods used to assemble different phases have been detailed in ref 28, and they are briefly described here. Polystyrene (PS) particles were synthesized using the dispersion polymerization method developed by Zhang *et al.*[67] A methanol and water mixture (130 mL:10 mL) is heated to 70 °C and then purged with argon gas for 5 min. Ten mL of sodium 4-vinylbezenesulfonate methanol (2.5 wt.%) is added to the flask, before adding 15 mL of styrene. The temperature is allowed to stabilize, at which point an initiator (10 mL 3 wt % azobisisobutyronitrile in methanol) is added, and the reaction is allowed to run to completion. After the particles are synthesized, they are cleaned a minimum of four times by centrifugation. The indium-tin oxide (ITO) slides (Sigma-Aldrich, Inc.) were prepared by sonication in acetone and isopropanol for 10 min each, before being cleaned by oxygen plasma for two minutes. The slides were then immersed and sonicated in a solution of 5 mg/mL polysodium 4-styrene sulfonate and 0.5 M potassium chloride for 10 min, before being rinsed with deionized (DI) water. The experiments were performed using an inverted microscope (Olympus IX71) with QImaging Retiga-2000R camera or a confocal microscope (Olympus FV 10i-W), and the AC electric fields were applied with a function generator (RTGOL DG1022).

A suspension of PS microspheres (diameter = 1.2 μm) dispersed in DI water was placed between two ITO glass slides that are separated by a plastic spacer of 100 μm. An AC electric field was then applied perpendicular to the two ITO electrodes, with voltage varying from 4 to 20 V peak-to-peak (V_{pp}) and frequency ranging from 700 Hz to 10 kHz. Although the electrode separation was large, the final structures near the bottom electrode were typically made of colloidal bilayers with variable γ.

ASSOCIATED CONTENT

Supporting Information

The Supporting Information is available free of charge at https://pubs.acs.org/doi/10.1021/acsnano.0c04939.

Polygon counting algorithm and additional figures (PDF)

AUTHOR INFORMATION

Corresponding Authors

Ning Wu − *Department of Chemical and Biological Engineering, Colorado School of Mines, Golden, Colorado 80401, United States;* orcid.org/0000-0002-2167-3621; Email: ningwu@mines.edu

David T. Wu − *Department of Chemistry, Colorado School of Mines, Golden, Colorado 80401, United States; Department of Chemical and Biological Engineering, Colorado School of Mines, Golden, Colorado 80401, United States;* orcid.org/0000-0002-1948-4565; Email: dwu@mines.edu

Authors

Joseph R. Maestas − *Department of Chemistry, Colorado School of Mines, Golden, Colorado 80401, United States*

Fuduo Ma − *Department of Chemical and Biological Engineering, Colorado School of Mines, Golden, Colorado 80401, United States*

Complete contact information is available at: https://pubs.acs.org/10.1021/acsnano.0c04939

Notes

The authors declare no competing financial interest.

ACKNOWLEDGMENTS

This work is supported by the National Science Foundation (CBET-1336893, CBET-2030480, and ECCS-1611330).

REFERENCES

(1) Bharti, B.; Kogler, F.; Hall, C. K.; Klapp, S. H. L.; Velev, O. D. Multidirectional Colloidal Assembly in Concurrent Electric and Magnetic Fields. *Soft Matter* **2016**, *12*, 7747−7758.

(2) Edwards, T. D.; Bevan, M. A. Controlling Colloidal Particles with Electric Fields. *Langmuir* **2014**, *30*, 10793−10803.

(3) Rechtsman, M. C.; Stillinger, F. H.; Torquato, S. Optimized Interactions for Targeted Self-Assembly: Application to a Honeycomb Lattice. *Phys. Rev. Lett.* **2005**, *95*, 228301.

(4) Bishop, K. J. M.; Wilmer, C. E.; Soh, S.; Grzybowski, B. A. Nanoscale Forces and Their Uses in Self-Assembly. *Small* **2009**, *5*, 1600−1630.

(5) Yang, T.; Tasci, T. O.; Neeves, K. B.; Wu, N.; Marr, D. W. M. Magnetic Microlassos for Reversible Cargo Capture, Transport, and Release. *Langmuir* **2017**, *33*, 5932−5937.

(6) Kudo, T.; Wang, S.-F.; Yuyama, K.; Masuhara, H. Optical Trapping-Formed Colloidal Assembly with Horns Extended to the Outside of a Focus through Light Propagation. *Nano Lett.* **2016**, *16*, 3058−3062.
(7) Luo, Y.; Serra, F.; Stebe, K. J. Experimental Realization of the "Lock-and-Key" Mechanism in Liquid Crystals. *Soft Matter* **2016**, *12*, 6027−6032.
(8) Park, K.; Koerner, H.; Vaia, R. A. Depletion-Induced Shape and Size Selection of Gold Nanoparticles. *Nano Lett.* **2010**, *10*, 1433−1439.
(9) Bharti, B.; Rutkowski, D.; Han, K.; Kumar, A. U.; Hall, C. K.; Velev, O. D. Capillary Bridging as a Tool for Assembling Discrete Clusters of Patchy Particles. *J. Am. Chem. Soc.* **2016**, *138*, 14948−14953.
(10) Mittal, M.; Lele, P. P.; Kaler, E. W.; Furst, E. M. Polarization and Interactions of Colloidal Particles in Ac Electric Fields. *J. Chem. Phys.* **2008**, *129*, 064513.
(11) Yang, Y.; Pham, A. T.; Cruz, D.; Reyes, C.; Wiley, B. J.; Lopez, G. P.; Yellen, B. B. Assembly of Colloidal Molecules, Polymers, and Crystals in Acoustic and Magnetic Fields. *Adv. Mater.* **2015**, *27*, 4725−4731.
(12) Lu, Y.; Yin, Y.; Xia, Y. Three-Dimensional Photonic Crystals with Non-Spherical Colloids as Building Blocks. *Adv. Mater.* **2001**, *13*, 415−420.
(13) Lee, S.; Lee, Y.-L.; Kim, B.; Kwon, K.; Park, J.; Han, K.; Lee, H.; Lee, W. Rapid On-Chip Integration of Opal Films and Photonic Gel Sensor Array *via* Directed Enhanced Water Evaporation for Colloidal Assembly. *Sens. Actuators, B* **2016**, *231*, 256−264.
(14) von Freymann, G.; Kitaev, V.; Lotsch, B. V.; Ozin, G. A. Bottom-Up Assembly of Photonic Crystals. *Chem. Soc. Rev.* **2013**, *42*, 2528−2554.
(15) Erb, R. M.; Libanori, R.; Rothfuchs, N.; Studart, A. R. Composites Reinforced in Three Dimensions by Using Low Magnetic Fields. *Science* **2012**, *335*, 199−204.
(16) Demirörs, A. F.; Courty, D.; Libanori, R.; Studart, A. R. Periodically Microstructured Composite Films Made by Electric- and Magnetic-Directed Colloidal Assembly. *Proc. Natl. Acad. Sci. U. S. A.* **2016**, *113*, 4623−4628.
(17) Ma, F.; Wang, S.; Wu, D. T.; Wu, N. Electric-Field−Induced Assembly and Propulsion of Chiral Colloidal Clusters. *Proc. Natl. Acad. Sci. U. S. A.* **2015**, *112*, 6307−6312.
(18) Ma, F.; Yang, X.; Zhao, H.; Wu, N. Inducing Propulsion of Colloidal Dimers by Breaking the Symmetry in Electrohydrodynamic Flow. *Phys. Rev. Lett.* **2015**, *115*, 208302.
(19) Wang, W.; Duan, W.; Ahmed, S.; Sen, A.; Mallouk, T. E. From One to Many: Dynamic Assembly and Collective Behavior of Self-Propelled Colloidal Motors. *Acc. Chem. Res.* **2015**, *48*, 1938−1946.
(20) Arpin, K. A.; Mihi, A.; Johnson, H. T.; Baca, A. J.; Rogers, J. A.; Lewis, J. A.; Braun, P. V. Multidimensional Architectures for Functional Optical Devices. *Adv. Mater.* **2010**, *22*, 1084−1101.
(21) Caleap, M.; Drinkwater, B. W. Acoustically Trapped Colloidal Crystals That Are Reconfigurable in Real Time. *Proc. Natl. Acad. Sci. U. S. A.* **2014**, *111*, 6226−6230.
(22) Trau, M.; Saville, D. A.; Aksay, I. A. Assembly of Colloidal Crystals at Electrode Interfaces. *Langmuir* **1997**, *13*, 6375−6381.
(23) Gong, T.; Wu, D. T.; Marr, D. W. M. Two-Dimensional Electrohydrodynamically Induced Colloidal Phases. *Langmuir* **2002**, *18*, 10064−10067.
(24) Saini, S.; Bukosky, S. C.; Ristenpart, W. D. Influence of Electrolyte Concentration on the Aggregation of Colloidal Particles near Electrodes in Oscillatory Fields. *Langmuir* **2016**, *32*, 4210−4216.
(25) Zhang, K.-Q.; Liu, X. Y. *In Situ* Observation of Colloidal Monolayer Nucleation Driven by an Alternating Electric Field. *Nature* **2004**, *429*, 739−743.
(26) Juárez, J. J.; Cui, J.-Q.; Liu, B. G.; Bevan, M. A. KT-Scale Colloidal Interactions in High Frequency Inhomogeneous AC Electric Fields. I. Single Particles. *Langmuir* **2011**, *27*, 9211−9218.
(27) Shah, A. A.; Kang, H.; Kohlstedt, K. L.; Ahn, K. H.; Glotzer, S. C.; Monroe, C. W.; Solomon, M. J. Liquid Crystal Order in Colloidal Suspensions of Spheroidal Particles by Direct Current Electric Field Assembly. *Small* **2012**, *8*, 1551−1562.
(28) Ma, F.; Wu, D. T.; Wu, N. Formation of Colloidal Molecules Induced by Alternating-Current Electric Fields. *J. Am. Chem. Soc.* **2013**, *135*, 7839−7842.
(29) Crocker, J. C.; Grier, D. G. Microscopic Measurement of the Pair Interaction Potential of Charge-Stabilized Colloid. *Phys. Rev. Lett.* **1994**, *73*, 352−355.
(30) Eral, H. B.; van den Ende, D.; Mugele, F.; Duits, M. H. G. Influence of Confinement by Smooth and Rough Walls on Particle Dynamics in Dense Hard-Sphere Suspensions. *Phys. Rev. E* **2009**, *80*, 061403.
(31) Bianchi, E.; Likos, C. N.; Kahl, G. Self-Assembly of Heterogeneously Charged Particles under Confinement. *ACS Nano* **2013**, *7*, 4657−4667.
(32) Ren, C.; Ma, Y. Phase Behavior in Thin Films of Confined Colloid−Polymer Mixtures. *J. Am. Chem. Soc.* **2006**, *128*, 2733−2737.
(33) Grandner, S.; Klapp, S. H. L. Freezing of Charged Colloids in Slit Pores. *J. Chem. Phys.* **2008**, *129*, 244703.
(34) Bowen, W. R.; Sharif, A. O. Long-Range Electrostatic Attraction between Like-Charge Spheres in a Charged Pore. *Nature* **1998**, *393*, 663−665.
(35) Han, Y.; Grier, D. G. Confinement-Induced Colloidal Attractions in Equilibrium. *Phys. Rev. Lett.* **2003**, *91*, 038302.
(36) French, R. H.; Parsegian, V. A.; Podgornik, R.; Rajter, R. F.; Jagota, A.; Luo, J.; Asthagiri, D.; Chaudhury, M. K.; Chiang, Y.; Granick, S.; Kalinin, S.; Kardar, M.; Kjellander, R.; Langreth, D. C.; Lewis, J.; Lustig, S.; Wesolowski, D.; Wettlaufer, J. S.; Ching, W.-Y.; Finnis, M.; Houlihan, F.; von Lilienfeld, O. A.; van Oss, C. J.; Zemb, T. Long Range Interactions in Nanoscale Science. *Rev. Mod. Phys.* **2010**, *82*, 1887−1944.
(37) Fontecha, A. B.; Schöpe, H. J.; König, H.; Palberg, T.; Messina, R.; Löwen, H. A Comparative Study on the Phase Behaviour of Highly Charged Colloidal Spheres in a Confining Wedge Geometry. *J. Phys.: Condens. Matter* **2005**, *17*, S2779−S2786.
(38) Pieranski, P.; Strzelecki, L.; Pansu, B. Thin Colloidal Crystals. *Phys. Rev. Lett.* **1983**, *50*, 900−903.
(39) Neser, S.; Bechinger, C.; Leiderer, P.; Palberg, T. Finite-Size Effects on the Closest Packing of Hard Spheres. *Phys. Rev. Lett.* **1997**, *79*, 2348−2351.
(40) Zhou, D.; Wang, F.; Li, B.; Lou, X.; Han, Y. Glassy Spin Dynamics in Geometrically Frustrated Buckled Colloidal Crystals. *Phys. Rev. X* **2017**, *7*, 021030.
(41) Gong, T.; Marr, D. W. M. Electrically Switchable Colloidal Ordering in Confined Geometries. *Langmuir* **2001**, *17*, 2301−2304.
(42) Osterman, N.; Babič, D.; Poberaj, I.; Dobnikar, J.; Ziherl, P. Observation of Condensed Phases of Quasiplanar Core-Softened Colloids. *Phys. Rev. Lett.* **2007**, *99*, 248301.
(43) Dobnikar, J.; Fornleitner, J.; Kahl, G. Ground States of Model Core-Softened Colloids. *J. Phys.: Condens. Matter* **2008**, *20*, 494220.
(44) Camp, P. J. Structure and Phase Behavior of a Two-Dimensional System with Core-Softened and Long-Range Repulsive Interactions. *Phys. Rev. E: Stat. Phys., Plasmas, Fluids, Relat. Interdiscip. Top.* **2003**, *68*, 061506.
(45) Schmidt, M.; Löwen, H. Freezing between Two and Three Dimensions. *Phys. Rev. Lett.* **1996**, *76*, 4552−4555.
(46) Hynninen, A.-P.; Dijkstra, M. Phase Behavior of Dipolar Hard and Soft Spheres. *Phys. Rev. E* **2005**, *72*, 051402.
(47) Bernard, E. P.; Krauth, W. Two-Step Melting in Two Dimensions: First-Order Liquid-Hexatic Transition. *Phys. Rev. Lett.* **2011**, *107*, 155704.
(48) Thompson, P. A.; Grest, G. S.; Robbins, M. O. Phase Transitions and Universal Dynamics in Confined Films. *Phys. Rev. Lett.* **1992**, *68*, 3448−3451.
(49) van der Meer, B.; Qi, W.; Sprakel, J.; Filion, L.; Dijkstra, M. Dynamical Heterogeneities and Defects in Two-Dimensional Soft Colloidal Crystals. *Soft Matter* **2015**, *11*, 9385−9392.

https://dx.doi.org/10.1021/acsnano.0c04939
ACS Nano 2021, 15, 2399−2412

(50) Edwards, T. D.; Yang, Y.; Beltran-Villegas, D. J.; Bevan, M. A. Colloidal Crystal Grain Boundary Formation and Motion. *Sci. Rep.* **2015**, *4*, 6132.
(51) Haghgooie, R.; Doyle, P. S. MR Fluid Structure in Quasi-2D. *Europhys. Lett. EPL* **2007**, *77*, 18002.
(52) Allen, M.; Tildesley, D. *Computer Simulations of Liquids*; Oxford University Press: New York, 1987.
(53) Humphrey, W.; Dalke, A.; Schulten, K. VMD: Visual Molecular Dynamics. *J. Mol. Graphics* **1996**, *14* (1), 33−38.
(54) Metropolis, N.; Rosenbluth, A. W.; Rosenbluth, M. N.; Teller, A. H.; Teller, E. Equation of State Calculations by Fast Computing Machines. *J. Chem. Phys.* **1953**, *21*, 1087.
(55) Chandler, D. *Introduction to Modern Statistical Mechanics*, 1st ed.; Oxford University Press: New York, 1987.
(56) Chen, Q.; Bae, S. C.; Granick, S. Directed Self-Assembly of a Colloidal Kagome Lattice. *Nature* **2011**, *469*, 381−384.
(57) Frank, F. C.; Kasper, J. S. Complex Alloy Structures Regarded as Sphere Packings. I. Definitions and Basic Principles. *Acta Crystallogr.* **1958**, *11*, 184−190.
(58) Frank, F. C.; Kasper, J. S. Complex Alloy Structures Regarded as Sphere Packings. II. Analysis and Classification of Representative Structures. *Acta Crystallogr.* **1959**, *12*, 483−499.
(59) Jones, T. B. *Electromechanics of Particles*; Cambridge University Press: Cambridge, 1995.
(60) Zhao, H. Double-Layer Polarization of a Non-Conducting Particle in an Alternating Current Field with Applications to Dielectrophoresis. *Electrophoresis* **2011**, *32*, 2232−2244.
(61) Zhou, H.; Preston, M. A.; Tilton, R. D.; White, L. R. Calculation of the Electric Polarizability of a Charged Spherical Dielectric Particle by the Theory of Colloidal Electrokinetics. *J. Colloid Interface Sci.* **2005**, *285*, 845−856.
(62) Shilov, V. N.; Delgado, A. V.; Gonzalez-Caballero, F.; Grosse, C. Thin Double Layer Theory of the Wide-Frequency Range Dielectric Dispersion of Suspensions of Non-Conducting Spherical Particles Including Surface Conductivity of the Stagnant Layer. *Colloids Surf., A* **2001**, *192*, 253−265.
(63) Schneider, C. A.; Rasband, W. S.; Eliceiri, K. W. NIH Image to ImageJ: 25 Years of Image Analysis. *Nat. Methods* **2012**, *9*, 671−675.
(64) Kwaadgras, B. W.; van Roij, R.; Dijkstra, M. Self-Consistent Electric Field-Induced Dipole Interaction of Colloidal Spheres, Cubes, Rods, and Dumbbells. *J. Chem. Phys.* **2014**, *140*, 154901.
(65) Vutukuri, H. R.; Smallenburg, F.; Badaire, S.; Imhof, A.; Dijkstra, M.; van Blaaderen, A. An Experimental and Simulation Study on the Self-Assembly of Colloidal Cubes in External Electric Fields. *Soft Matter* **2014**, *10*, 9110−9119.
(66) Yang, X.; Johnson, S.; Wu, N. The Impact of Stern-Layer Conductivity on the Electrohydrodynamic Flow Around Colloidal Motors under an Alternating Current Electric Field. *Adv. Intell. Syst.* **2019**, *1*, 1900096.
(67) Zhang, F.; Cao, L.; Yang, W. Preparation of Monodisperse and Anion-Charged Polystyrene Microspheres Stabilized with Polymerizable Sodium Styrene Sulfonate by Dispersion Polymerization. *Macromol. Chem. Phys.* **2010**, *211*, 744−751.

https://dx.doi.org/10.1021/acsnano.0c04939
ACS Nano 2021, 15, 2399−2412